Photofragmentation spectra and structures of Sr^+Ar_n, $n=2-8$ clusters: Experiment and theory

G. S. Fanourgakis,[a] S. C. Farantos,[a] Ch. Lüder, and M. Velegrakis
Institute of Electronic Structure and Laser, Foundation for Research and Technology – Hellas, Iraklion, Crete 711 10, Greece

S. S. Xantheas
Environmental Molecular Sciences Laboratory, Pacific Northwest National Laboratory, 906 Battelle Boulevard, P.O. Box 999, MS K1-96, Richland, Washington 99352

(Received 26 January 1998; accepted 27 March 1998)

The total photofragmentation cross sections of size selected Sr^+Ar_n, $n=2-8$, clusters have been recorded in a time of flight (TOF) mass spectrometer. In the energy range of 21 000–27 000 cm^{-1} three absorption bands are observed that are attributed to transitions from the ground to the three excited states that correlate to the $5p$ orbitals of strontium. No vibrational structure in the spectral bands is observed, even in regions where the spectrum is recorded with a resolution of 1 cm^{-1}. The absorption spectra are calculated within a semiclassical approximation. Accurate *ab initio* calculations for the ground $X\ ^2\Sigma$ and the $A\ ^2\Pi$ and $B\ ^2\Sigma$ excited states of Sr^+Ar are combined with a perturbative one-electron model, which includes the spin–orbit coupling, to construct potential energy surfaces for the excited states of all clusters. The theoretical spectra obtained without using any adjustable parameters reproduce the patterns and trends of the experimental spectra, but they are shifted to higher frequencies. A better agreement between theoretical and experimental spectra is obtained by adjusting the depth of the potential wells of the ground $X\ ^2\Sigma$ and excited $A\ ^2\Pi$ states of the Sr^+Ar dimer to the experimentally estimated values. From both calculations we conclude that Sr^+Ar_3 is a trigonal pyramid of C_{3v} symmetry and Sr^+Ar_6 has a C_{5v} symmetry with five argon atoms forming a regular pentagon, one argon atom below and the cation above the pentagon plane. For these clusters, theory reproduces the characteristic blue shifts found in the absorption spectra and the splittings of the doubly degenerate states encountered in these symmetric complexes. [S0021-9606(98)02125-4]

I. INTRODUCTION

The purpose of this study is to extract information about the structures of Sr^+Ar_n, $n=2-8$, clusters via the study of their photofragmentation spectra recorded after the absorption of photons in the energy range of 21 000–27 000 cm^{-1}. These complexes are produced and detected in a time of flight (TOF) mass spectrometer from which the stoichiometry of the clusters is deduced. From the intensities in the mass spectrum, the most stable (magic numbers) clusters are identified and structural information may be obtained by comparing them to previously studied complexes whose geometries are known. Obviously, such knowledge is only indicative and supplementary spectroscopic studies are required for a more definitive characterization of the cluster structures. Metal ion doped inert gas clusters, such as Sr^+Ar_n, offer the advantage of having the metal cation acting as a chromophore species, and, therefore, information about the bonding of metal ion to the noble gas atoms can be deduced by studying their fragments. Such an approach demands the parallel development of a theoretical model for the interpretation of the observed spectra.

We build on the previous work of the photofragmentation of the Sr^+Ar dimer recently reported by Lüder and Velegrakis.[1] From the experimental spectra measured over the wavelength range of 418–448 nm, spectroscopic constants were obtained for the ground, $X\ ^2\Sigma_{1/2}$, and the excited $A\ ^2\Pi_{1/2}$ and $A\ ^2\Pi_{3/2}$ states. The vibrational progressions found in these spectra provided estimates of the dissociation energies, the harmonic frequencies, and the anharmonic constants. However, due to the lack of rotational progressions in the observed spectra, it was not possible to extract the equilibrium separations in the two states.

This work has stimulated our recent theoretical study, which involves accurate *ab initio* calculations of the potential energy curves for the ground, $X\ ^2\Sigma^+$, and the excited $A\ ^2\Pi$ states[2] of the dimer. These states arise from the interaction of a ground state $Ar(^1S)$ with the electron in the $5s$ or $5p$ orbitals of Sr, respectively. The ground state electronic configuration of the strontium cation is $[Kr]5s$.[1] The $4d$ orbitals of Sr are lying higher in energy producing the $^2D_{3/2}$ (14 555.9 cm^{-1}) and $^2D_{5/2}$ (14 836.2 cm^{-1}) excited states, respectively, when the spin–orbit coupling is included.[3] The states originated from the $5p$ orbitals of Sr lie at 23 715.2 ($^2P_{1/2}$) and 24 516.6 ($^2P_{3/2}$) cm^{-1} above the ground state. The spin–orbit interaction energy[3] in this case is about 800 cm^{-1}.

[a]Also at: The Department of Chemistry, University of Crete.

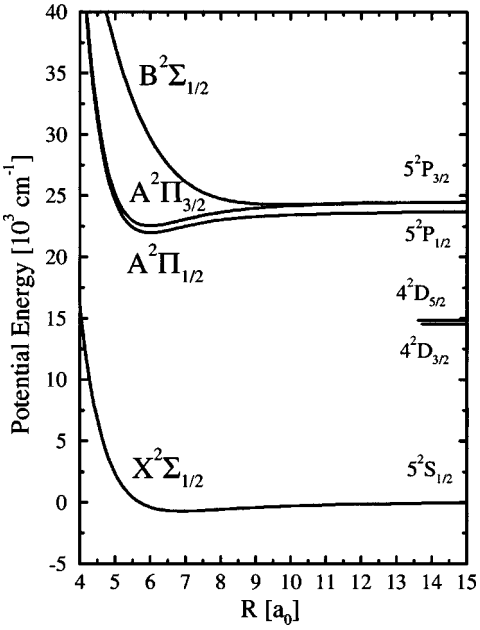

FIG. 1. Potential energy curves for the ground and the $^2\Pi$ and $^2\Sigma$ excited states of the Sr^+Ar dimer that correlate with the $Sr^+(5^2P)+Ar(^1S)$ dissociation channel. The energy is measured with respect to the free atomic species in their ground state. In the figure the energy position of the $Sr^+(4^2D)+Ar(^1S)$ asymptotic channels are shown.

The approach of an Ar atom to the ground state Sr^+ will result in the $X\ ^2\Sigma_{1/2}$ ground electronic state, whereas its interaction with the $4d$ orbitals of strontium yields one Σ, one Π, and one Δ state, respectively. Finally, its interaction with the $5p$ orbitals gives rise to what we call $A\ ^2\Pi$ and $B\ ^2\Sigma$ states of Sr^+Ar. A schematic representation of the potential curves is shown in Fig. 1. The measured photofragmentation spectra resulted from the transitions $X\ ^2\Sigma_{1/2}\rightarrow A\ ^2\Pi_{1/2,\,3/2}$.

Spectroscopic studies have been carried out for all alkaline earth metal ion–argon dimers, except for the radioactive radium.[4–12] Dissociation energies, harmonic frequencies, anharmonic constants, and, in a few cases, equilibrium bond lengths have experimentally been determined. An analysis of these results reveals that charge-induced dipole-type interactions are sufficient to explain the trends in the data.[1,12–15]

In spite of the proliferation of results in the alkaline earth–inert gas dimers,[16–18] larger size clusters are less studied. The present work is our first effort to investigate more complex systems such as the Sr^+Ar_n aggregates. An even more ambitious goal is to use inert gas clusters doped with metal cations as prototype systems for exploring solvation effects on a microscopic scale. Extending such efforts to studies of metal ions with conventional molecules, water, for example,[19–22] leads to a better understanding of catalytic phenomena in biological systems. The ionic character of the complexes allows for the mass separation and subsequent selection of the fragments after dissociation of the isolated clusters with a laser.

The paper is organized as follows: in Sec. II we describe the experimental setup and summarize the conclusions drawn from the observed spectra. In Secs. III and IV we present the potential energy surfaces of the involved electronic states and the computational methods used to derive them. In these two sections we outline the basic equations and discuss in detail the assumptions made for an effective and practical way to compute the spectra at several temperatures for these complex systems. We have decided to present these details at this point in the article so the reader can better evaluate the results given in Sec. V. A discussion of the results is presented in Sec. VI, and the main conclusions are summarized in Sec. VII.

II. EXPERIMENT

The molecular beam apparatus used for the photofragmentation experiments has been described in detail previously.[1] The setup consists of a cluster ion source and a double focusing time of flight mass spectrometer. The Sr^+Ar_n clusters are formed in a laser vaporization source, where the focused light of a pulsed infrared Nd:YAG laser ($\lambda=1064$ nm, pulse duration 10 ns, repetition rate 12.5 Hz) produces a plasma from a pure strontium target. The plasma is injected into a supersonic stream of Ar gas provided by a pulsed nozzle (diameter 0.8 mm, backing pressure 5 bar, room temperature). Due to association reactions in a region of a high number of collisions between noble gas atoms and the Sr ions contained in the plasma, cluster growth is achieved. The clusters are then cooled and stabilized by collisions within the expanding gas. After passing a skimmer, the ions are accelerated by a pulsed two-field Wiley–McLaren setup.[23] The spatial focus of this device is adjusted to lie approximately 1 m downstream from the last grid, at the position of a two-plate mass selector, which rejects the undesired ions and allows the transmission of the selected ones toward the reflectron assembly. Finally, the reflected ions are focused into a microchannel plate detector (MCP), where TOF mass spectra can be recorded with a computer controlled digital storage oscilloscope. The pulsed nozzle, the ablation laser firing, the triggering of the TOF, and the mass gate are synchronized through coupled delay generators, which are sequentially optimized for a maximum signal.

In order to record photofragmentation spectra of selected masses, a tunable pulsed dye laser (at collinear arrangement with the ion beam) is fired when the ions under investigation are located in the mass gate. The photofragments are separated in the TOF spectrum from the parent masses as due to the conservation of energy. The fragments that have lower kinetic energy penetrate less deeply into the reflectron, and consequently arrive earlier at the MCP detector.

It should be mentioned that in this collinear setup where the fragmentation happens in between the mass gate is chosen as the more appropriate in our case since the experimental results are reproducible. The mass resolution of the fragment channels, however, is limited, especially for fragments arising from big clusters, since these fragments are reflected already from the first (retarding) field of the reflectron assembly. Other fragmentation schemes, such as firing the laser when the ions are located at their turning point in the reflectron, although exhibit improved resolution, suffers from reproducibility. This is caused by the fluctuations of the laser–ion beam overlap.

Assuming (i) an exponential attenuation of the ion beam after the photoexcitation and (ii) that each absorbed photon

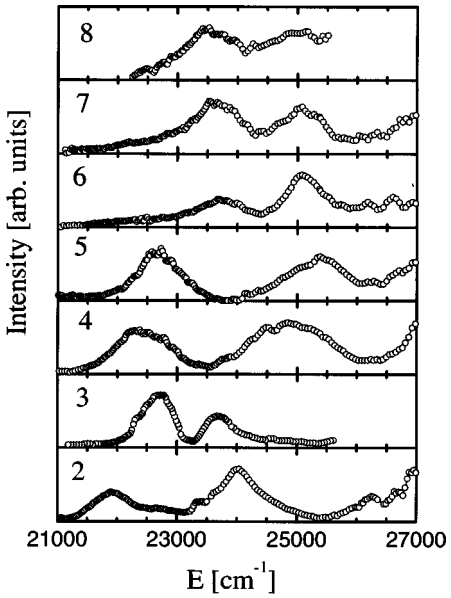

FIG. 2. The experimental photofragmentation spectra of Sr^+Ar_n, $n=2-8$, clusters. The horizontal axis corresponds to the fragmentation laser frequency while the vertical axis represents the intensity ratio of the sum of all ionic fragments to the total normalized by the dye intensity. The two bands and an emerging one at higher frequencies are assigned to transitions from the ground state to the three states that correlate with the $Sr^+(5^2P)+nAr(^1S)$ dissociation channel.

leads at least to one evaporation event in the time window of the measurement (~ 10 μs), then the photofragmentation cross section is equal or constitutes a lower limit for the photoabsorption cross section. Thus, the fragmentation data are evaluated according to Beer's law:

$$D=1-A+A\ \exp[-(\sigma_1+\sigma_2+\cdots)\Phi-\alpha]. \tag{1}$$

with $D=I_P/(I_P+I_{F_1}+I_{F_2}+\cdots)$. $I_P, I_{F_1}, I_{F_2}, \ldots,$ are the integrated peak intensities of the parent ion and its fragments, respectively, $\sigma_1, \sigma_2 \ldots,$ are the (laser wavelength-dependent) photofragmentation cross sections, α denotes a decay rate due to collisions of the mass selected parent with the reflectron grids and/or the background gas, Φ is the laser fluence (photons/cm^2), and A is a geometrical factor that represents the overlap between the laser beam and the ion beam.

For each laser wavelength the mass spectrum has been recorded with the dissociation laser ON and OFF to account for the fragmentation that is not due to the laser interaction. Thus, for perfect overlapping ($A=1$) the total photofragmentation cross section is

$$\sigma_{\text{tot}}=\sigma_1+\sigma_2+\cdots=-[\ln(D_{\text{on}})+\ln(D_{\text{off}})]/\Phi. \tag{2}$$

The photofragmentation spectra of $Sr^+Ar_n, n=2-8$, clusters are shown in Fig. 2. The total photofragmentation cross section [Eq. (2)] as a function of the photon energy is plotted. Using the atomic absorption energies of a strontium cation, it was concluded in the earlier study of the dimer that the absorption bands result from the electronic transitions $X\ ^2\Sigma_{1/2}\rightarrow A\ ^2\Pi_{1/2,3/2}$. Further tests on Sr^+Ar and Sr^+Ar_2 did not show any fragmentation in the region of 13 800–14 000 cm^{-1}, where the states that correlate to the d orbitals of strontium are expected.

From Fig. 2 we make the following remarks:

(1) In the energy range in which the spectra are obtained, all clusters show two absorption bands, whereas a third one starts to appear at higher energies, although not fully uncovered.

(2) No vibrational structure is observed, in spite of using resolution of 1 cm^{-1} in certain regions of the spectrum.

(3) For Sr^+Ar_2 we see two bands separated by about 2000 cm^{-1}, at 22 000 and 24 000 cm^{-1}, respectively. A third one extends beyond 27 000 cm^{-1}.

(4) The next size cluster, Sr^+Ar_3, shows a significant variation in its spectral pattern with the two first bands approaching each other and separated now only by 1000 cm^{-1}. The first peak shows a blue shift and the second a red shift compared to Sr^+Ar_2. Both bands are significantly narrower than the bands of the other complexes.

(5) Moving to Sr^+Ar_4, the separation of the first two peaks increases again (about 2500 cm^{-1}), with the first peak slightly red shifted and the second peak blue shifted by 1500 cm^{-1} with respect to Sr^+Ar_3. A third peak extends beyond 27 000 cm^{-1}.

(6) For Sr^+Ar_5, we do not see any significant change apart from a blue shift of 500 cm^{-1} in the second band compared to the previous complex. For both aggregates with four and five Ar atoms, the widths of the bands increase.

(7) Another significant variation in the photofragmentation spectrum is observed for Sr^+Ar_6. In Fig. 2 we can see a 1200 cm^{-1} blue shift of the first peak compared to that of Sr^+Ar_5. As a matter of fact three peaks come close to one another and cover an energy range from 21 000 to 27 000 cm^{-1}. The first band shows a shoulder on the left side whereas the third band seems to be composed by a few peaks.

(8) For the larger clusters, Sr^+Ar_7 and Sr^+Ar_8, the spectra resemble those of Sr^+Ar_6 and the only difference is a slight red shift of the first peak.

Summarizing our observations, we find a significant blue shift of the first band in Sr^+Ar_3 and Sr^+Ar_6 compared to smaller size clusters. We attribute this behavior as well as the other remarks made above largely to structural changes and to a lesser extent to shifts of corresponding energy levels due to the addition of Ar atoms to the cluster. In the remainder of the paper we present theoretical efforts for modeling the electronic spectra and the elucidation of the structures and dynamics of the clusters. To accomplish this goal, we must first construct the appropriate multidimensional potential energy surfaces (PES), a topic that will be addressed in the next section.

III. POTENTIAL ENERGY SURFACES

Accurate *ab initio* PES for the larger strontium–argon clusters cannot be constructed at present. We have therefore opted to employ approximate theories in order to obtain potential functions for the ground and the excited states of $Sr^+Ar_n, n=2-8$, aggregates. For the states that correlate with the $5p$ orbitals of the metal atom, a successful model

has been previously proposed by Baylis.[24] The Baylis' model treats the metal ion as a one-electron system, assuming an effective potential for the core electrons, while the interactions of the single electron with closed shell atoms are described by first-order perturbation theory.

The model has been applied to several systems since it was introduced. Balling and Wright[25] used it to describe the interactions of alkali atoms with rare gas in matrices. Harima *et al.*[26] investigated the alkaline earth metal ion–rare gas atom dimers. One of the systems studied was Sr^+Ar. A comparison of their results with the experiment[1] and our earlier *ab initio* study[2] revealed large discrepancies that we attributed to the empirical parameters that they used to compute the potential energy curves. In particular, the empirical calculations underestimate the dissociation energy of the excited $A\ ^2\Pi$ states by about 1000 cm^{-1} (or 40%) as well as the shift in the equilibrium separation between the ground $X\ ^2\Sigma$ and the $A\ ^2\Pi$ excited states by $0.28a_0$.

More recently, Boatz and Fajardo[27] studied the structures and optical absorption spectra of sodium neutral atoms in Ar clusters using Monte Carlo simulations. Lawrence and Apkarian[28] applied the same procedure to study the interaction of a hole in the p orbitals (iodine) with Kr and Xe. Another application of Baylis' perturbative model has been described by Alexander *et al.*[29] for the $2p \rightarrow 3s$ electronic excitation spectrum in the BAr and BAr_2 complexes.

In the cited literature several approaches have been taken in formulating the interaction of an atom with a closed core and an electron or a hole in p orbitals with closed shell atoms. In our case we follow the Lawrence and Apkarian[28] formulation.

The Hamiltonian is defined by the equation

$$H = H_A(\mathbf{r}) + V_{Sr^+Ar}(\mathbf{r},\mathbf{R_1},\mathbf{R_2},\ldots,\mathbf{R_n}), \tag{3}$$

where

$$V_{Sr^+Ar}(\mathbf{r},\mathbf{R_1},\mathbf{R_2},\ldots,\mathbf{R_n}) = \sum_{k=1}^{n} V(\mathbf{r},\mathbf{R}_k). \tag{4}$$

$H_A(\mathbf{r})$ is the Hamiltonian of the free metal ion and $V(\mathbf{r},\mathbf{R}_k)$ denotes the interaction potential between the p electron at the position $\mathbf{r}$ and the kth argon atom, which is located at the position $\mathbf{R}_k$. We take the nucleus of the metal ion as the origin of the coordinate system. By summing over all argon atoms k the total interaction potential, V_{Sr^+Ar}, is computed.

Assuming that ϵ_i are the eigenenergies of the free ion and ψ_i the minimal basis set that consists of the product of the $5p$ orbitals of strontium with one s-type orbital of argon, the eigenenergies E of the cluster are found by solving the equation

$$\det|V_{ij} - (\epsilon_i - E)\,\delta_{ij}| = 0, \tag{5}$$

where the matrix element V_{ij} are defined by

$$V_{ij} = \sum_k \langle \psi_i | V(\mathbf{r},\mathbf{R}_k) | \psi_j \rangle. \tag{6}$$

The angular dependence of V_{Sr^+Ar} can be expanded in Legendre polynomials, P_L:

$$V_{Sr^+Ar}(\mathbf{r},\mathbf{R_1},\mathbf{R_2},\ldots,\mathbf{R_n}) = \sum_{k=1}^{n} \sum_{L=0}^{\infty} V_L(r,R_k) P_L(\mathbf{R}_k \cdot \mathbf{r}). \tag{7}$$

For the particular case of $l=1$ that concerns us, the only terms that survive in the Legendre expansion are V_0 and V_2. Thus, the matrix elements V_{ij} become

$$V_{m_l m_l'} = \sum_{k=1}^{n} \langle p | V_0(r,R_k) | p \rangle \langle m_l | P_0(\mathbf{r}\cdot\mathbf{R}_k) | m_l' \rangle, \tag{8}$$

$$+ \sum_{k=1}^{n} \langle p | V_2(r,R_k) | p \rangle \langle m_l | P_2(\mathbf{r}\cdot\mathbf{R}_k) | m_l' \rangle. \tag{9}$$

In this equation the radial part is separated from the angular one in the integration. The latter is computed by using spherical harmonics, $|lm_l\rangle$.[28]

The next step is to express the R dependence of the coefficients, $\langle V_0(r,R)\rangle$ and $\langle V_2(r,R)\rangle$, in terms of Sr^+Ar diatomic potential energy curves,[30] V_Π and V_Σ:

$$V_0(R) = \langle V_0(r,R)\rangle = \tfrac{1}{3}[V_\Sigma(R) + 2V_\Pi(R)], \tag{10}$$

$$V_2(R) = \langle V_2(r,R)\rangle = \tfrac{5}{3}[V_\Sigma(R) - V_\Pi(R)]. \tag{11}$$

The spin–orbit interaction H_{so},

$$H_{so} = (\tfrac{2}{3}\Delta)\mathbf{l}\cdot\mathbf{s}, \tag{12}$$

can be added in the Hamiltonian of Eq. (3) and then the functions $|jm_j\rangle$ are used as a basis set. $\mathbf{l}$ is the orbital angular momentum, $\mathbf{s}$ is the total spin, and Δ is the spin–orbit splitting of the free Sr^+ ($^2P_{3/2} - {}^2P_{1/2}$). $\mathbf{j}$ is the sum of the orbital angular momentum and spin, and m_j the projection of $\mathbf{j}$ on the z axis. The eigenenergies are then obtained by diagonalizing a 6×6 matrix, $V_{m_j m_j'}$.[31]

The potential energy surfaces for the ground electronic states are constructed as pairwise additive potentials:

$$E_g(\mathbf{q}) = \sum_k V_{Sr^+Ar}(|\mathbf{R}_k|) + \sum_k \sum_{l<k} V_{ArAr}(|\mathbf{R}_l - \mathbf{R}_k|), \tag{13}$$

where V_{Sr^+Ar} denotes the Sr^+–Ar ground state potential, and V_{ArAr} the Ar–Ar interaction. The indices k and l run over all Ar atoms. $\mathbf{q}$ collectively denotes all the internuclear coordinates. The zero of energy is defined with respect to all separated atoms. For the Ar–Ar potential we use the empirical model of Aziz and Slaman[32] that we have used before in several applications.[33]

IV. COMPUTATIONAL METHODS

A. *Ab initio* calculations

What makes Baylis' model so successful is the transformation from the Legendre coefficients to the potential curves of the dimer via Eqs. (10)–(11). From the analysis in Secs. I and III it is apparent that the potential curves for the ground Σ, and the excited states Σ and Π are needed. These may be obtained independently, either from empirical or *ab initio* calculations. In our case the potential curves were obtained using the internally contracted multireference single and double excitation configuration interaction (icMRCI)

TABLE I. Comparison of experimental and *ab initio* results for the spectroscopic constants of Sr^+Ar in the ground and excited states. D_0 is the dissociation energy, R_e the equilibrium bond length, ω_e the harmonic frequency, and $\omega_e\chi_e$ the anharmonicity. All units are in cm^{-1} except the distances that are in Bohr. The spectroscopic constants were extracted via a Dunham analysis using points around the minimum. The numbers in parentheses are the results of the fits using Extended Rydberg Functions (ERF; see the text).

	D_0	R_e	ω_e	
	Ground	state	($X\ ^2\Sigma$)	$\omega_e\chi_e$
Experiment	803±244	⋯	49.5	0.75
icMRCI	603	7.009	35.2	0.64
icMRCI+Q	675 (683)	6.920 (6.899)	38.7 (42.75)	0.72 (0.896)
RCCSD(T)	685	6.856	39.9	0.67
	Excited	state	($A\ ^2\Pi$)	
Experiment ($A\ ^2\Pi_{1/2}$)	2303±232	⋯	120.8±0.5	1.67±0.04
Experiment ($A\ ^2\Pi_{3/2}$)	2575±256	⋯	122±0.5	1.6±0.04
icMRCI ($A\ ^2\Pi$)	1767	6.015	95.8	1.61
icMRCI+Q ($A\ ^2\Pi$)	1918 (1923)	5.989 (5.996)	99.1 (99.2)	1.57 (1.45)

method[34–37] from a multiconfiguration self-consistent field (MCSCF) wave function. The MCSCF calculations were performed in the configuration space of $17e^-$ in 12 orbitals. Within this active space we have performed a four-state average MCSCF calculation (15 128 CSFs) with equal weights for the ground state, the $^2\Sigma$ and $^2\Delta$ states coming from the $Sr^+(4d)$ orbitals, and the repulsive $B\ ^2\Sigma$ state arising from the $Sr^+(5p)$ orbitals and subsequently successive projected icMRCI calculations for four states. The states of Π symmetry were obtained by a similar procedure, viz. a two-state average MCSCF (14 204 CSFs) and subsequent projected icMRCI calculations for two states. The corresponding number of internally contracted CSFs in the icMRCI is 2 140 732 for the $l=0$ and 2 122 179 for the $l=1$ states out of about 135 million uncontracted. Details can be found elsewhere.[2]

In order to evaluate the accuracy of the icMRCI method for this system we have also performed coupled cluster calculations, including single and double excitations with a perturbative estimation of the triple excitations [RCCSD(T)] from a restricted Hartree–Fock (RHF) reference wave function for the $X\ ^2\Sigma$ ground state correlating 17 electrons. The dissociation limit for the separated atoms was calculated using the supermolecule approach at the icMRCI (the energy is computed at an internuclear separation of $100a_0$) and the sum of the separated atoms at the RCCSD(T) levels of theory, respectively.

For the Sr atom basis set we used the quasirelativistic effective core potential (ECP) from the Stuttgart group[38] (28 core electrons) in conjunction with the $(6s6p5d)$ valence set contracted to $[4s4p2d]$ for the remaining electrons. For Ar we used the doubly augmented correlation-consistent polarized valence double zeta (d-aug-cc-pVDZ) basis set.[39] This consists of the regular aug-cc-pVDZ set[40–42] augmented with one additional diffuse function of each symmetry (s,p,d) whose exponents are determined in an even-tempered fashion. All calculations were performed using the MOLPRO program suite.[43]

We used two schemes in order to obtain the spectroscopic constants, i.e., the equilibrium bond length (R_e), the dissociation energy (D_e), the harmonic frequency (ω_e), and the anharmonicity $(\omega_e\chi_e)$. The first scheme incorporated a Dunham analysis using points around the minimum. The second approach involved the use of Extended Rydberg Functions (ERF)[44] in order to represent the ground and the excited Σ and Π potential curves:

$$V(R) = -D_e(1+\alpha_1\rho+\alpha_2\rho^2+\alpha_3\rho^3)\exp(-\alpha_1\rho), \quad (14)$$

where

$$\rho = R - R_e\,. \quad (15)$$

The spectroscopic constants obtained with the two different functions are shown in Table I, together with the experimental estimates. The numbers in parentheses correspond to fits with the ERF. In the icMRCI calculations, the +Q designation denotes the multireference analog[45] of the Davidson correction[46] that provides an estimate of higher-than-double excitations from the MCSCF active space. We have chosen to fit the icMRCI+ Q energies to the ERF, since these results are much closer to the ones obtained at the RCCSD(T) level of theory for the ground state. The five parameters, D_e, R_e, a_1, a_2, a_3, fitted using the icMRCI+Q points, are listed in Table II.

The results of Table I indicate that the ERF fits produce a dissociation energy in the ground state that is underestimated compared to the experimental value by about 100 cm^{-1}, whereas the difference is 400–600 cm^{-1} in the Π state. Our best estimate for the harmonic frequency of the excited state is about 20 cm^{-1} lower than the one determined

TABLE II. The values of the fitted parameters in the Extended Rydberg Functions (ERF) to *ab initio* calculations for the ground and the excited states of Sr^+Ar. D_e is the dissociation energy, R_e the equilibrium bond length, and α_i, $i=1-3$, the coefficients in the polynomial. The numbers in parentheses are the corresponding values for the modified ERFs (mERF; see the text).

	D_e (cm^{-1})	$R_e(a_0)$	α_1 (a_0^{-1})	α_2 (a_0^{-2})	α_3 (a_0^{-3})
$X\ ^2\Sigma$	704.28	6.90	0.818 72	0.037 378 1	0.043 465 9
	(828)	6.90	(0.818 72)	(-0.004 50)	(0.043 465 9)
$A\ ^2\Pi$	1972.54	6.00	0.897 26	−0.170 039 1	0.068 638 7
	(2636)	(6.00)	(0.897 26)	(−0.245 53)	(0.068 638 7)
$B\ ^2\Sigma$	165.95	10.16	0.836 78	0.085 560 2	0

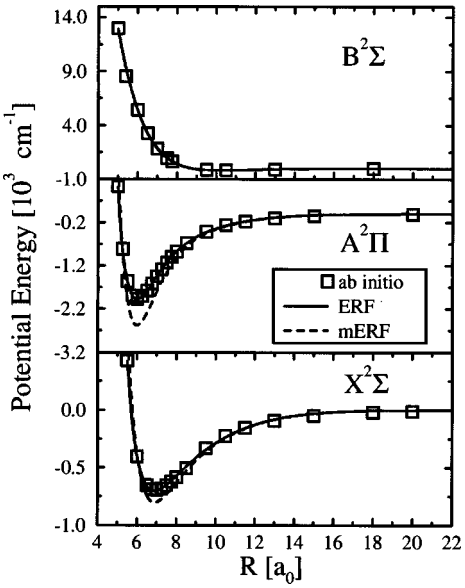

FIG. 3. The *ab initio* points (squares) and the Extended Rydberg Function (ERF) curves (solid). The dashed line curves represent the modified Extended Rydberg Functions (mERF) that reproduce the experimentally estimated binding energies of the dimer for the ground (828 cm^{-1}) and the excited $A\ ^2\Pi$ states (2636 cm^{-1}).

experimentally, and 7 cm^{-1} lower for the ground state. The calculated *ab initio* points and the fitted potentials are shown in Fig. 3. In this figure the translation of the minimum in the $A\ ^2\Pi$ state to smaller R values by $0.94a_0$ and the repulsive character of the $B\ ^2\Sigma$ potential can be clearly seen. The dashed lines shown in the same figure for the two attractive potentials represent modified ERFs with the same equilibrium bond lengths, but fitted to the experimentally estimated dissociation energies. We label these potential curves as mERF. The corresponding mERF parameters are the numbers in the parentheses of Table II.

B. Absorption spectra

To compute the absorption spectra we apply the classical Franck–Condon method,[47–49] which has successfully been used in the past.[27,28] According to this semiclassical model, we evaluate the total absorption spectrum from the formula

$$I(\omega)\propto\int d\mathbf{q}P(\mathbf{q})\delta[(V_f(\mathbf{q})-V_i(\mathbf{q}))/\hbar-\omega], \tag{16}$$

where ω is the laser frequency, and $V_i(\mathbf{q})$ and $V_f(\mathbf{q})$ are the potential functions of the initial and final state, respectively. $P(\mathbf{q})$ is a classical statistical mechanical configurational probability distribution. Assuming electric dipole transition moments, this distribution originates from the ground electronic state $\phi(\mathbf{q})$, $\psi=\hat{\mu}\phi$; $\hat{\mu}$ is the dipole moment operator. By making the assumption of a coordinate independent dipole moment, the distribution $P(\mathbf{q})$ is the classical analog of ϕ^2. Heller[49] has discussed the validity of the above formula and its limitations for polyatomic molecules.

Another assumption that is made by applying Eq. (16) is to consider a constant density of states in the upper electronic state.[28] We should notice that in Eq. (16) we integrate the delta function with respect to coordinates and not with respect to the total energy. Therefore, we should replace the delta function by

$$\delta[(V_f(\mathbf{q})-V_i(\mathbf{q}))/\hbar-\omega]=\sum_i\frac{\delta(\mathbf{q}-\mathbf{q}_i)}{|\nabla(V_f-V_i)|_{\mathbf{q}_i}}, \tag{17}$$

where $\mathbf{q_i}$ are the roots of the factor inside the δ function in the left side of the equation. We assume that the $|\nabla(V_f-V_i)|_{\mathbf{q}_i}$ is constant.

For the implementation of the above method the classical statistical mechanical probability, $P(\mathbf{q})$, is computed by running trajectories on the ground electronic state at constant temperatures using the Nosé–Hoover technique.[50–52] This method was chosen since in the experiment it is not possible to know the temperature of clusters. Therefore, we carry out calculations at several temperatures before comparing with the experimental spectra.

According to the Nosé–Hoover technique, the cluster is coupled to a heat bath via the coordinate s, such that the temperature of the system is kept fixed and is defined from the average kinetic energy:

$$kT_{\rm kin}=2\left\langle\sum_i\mathbf{p}_i^2/(2m_i)\right\rangle\Big/\,g. \tag{18}$$

$\mathbf{p}_i$ are the conjugate momenta to coordinates $\mathbf{q}_i$, k is the Boltzmann constant, m_i the atomic masses, and g the number of degrees of freedom.

The temporal evolution of the system is followed by integrating the equations:

$$\frac{d\mathbf{q}_i}{dt}=\frac{\mathbf{p}_i}{m_i}, \tag{19}$$

$$\frac{d\mathbf{p}_i}{dt}=-\frac{\partial V}{\partial\mathbf{q}_i}-\zeta\mathbf{p}_i, \tag{20}$$

$$\frac{Q}{2}\frac{d\zeta}{dt}=\sum_i\frac{\mathbf{p}_i^2}{2m_i}-\frac{g}{2}kT. \tag{21}$$

ζ is related to the coupling coordinate s according to the equation

$$\frac{d\ \ln s}{dt}=\zeta. \tag{22}$$

Q is a mass-like factor that determines the degree of the system–bath coupling. Equation (21) controls the fluctuations of the energy of the system such that the temperature is kept fixed.

The trajectories at a specified temperature are integrated on the ground potential energy surface for 15 ns and with zero total angular momentum. At constant time steps we compute the potential energy differences between the ground and the three excited electronic states. The results are then used to plot the distributions of these vertical energy differences as functions of total energy. The range of temperatures that we have examined is from 10 to 60 K.

We have performed additional calculations in order to search for minima on the ground potential energy surface by

Sr^+Ar_2 (C_{2v})	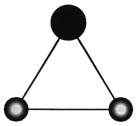	$E_g = -1508$ 22582 (22636) 24563 (24542) 27962 (27930)	$E_g = -1755$ 21964 (22012) 24167 (24148) 27976 (27947)
Sr^+Ar_3 (C_{3v})	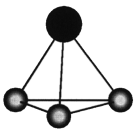	$E_g = -2411$ 23442 (23735) 24003 (23735) 28844 (28817)	$E_g = -2782$ 22739 (23030) 23297 (23030) 28751 (28727)
Sr^+Ar_4 (C_{2v})	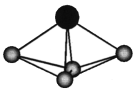	$E_g = -3322$ 22887 (22924) 26056 (26057) 28530 (28491)	$E_g = -3817$ 21874 (21908) 25410 (25412) 28183 (28147)
Sr^+Ar_5 (C_s)	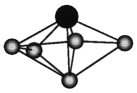	$E_g = -4240$ 23646 (23686) 27166 (27250) 27854 (27730)	$E_g = -4858$ 22504 (22540) 26450 (26527) 27196 (27084)
Sr^+Ar_6 (C_{5v})	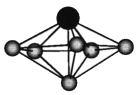	$E_g = -5257$ 26014 (26422) 26689 (26422) 27166 (27025)	$E_g = -5999$ 24980 (25376) 25643 (25376) 26216 (26087)
Sr^+Ar_7 (C_s)	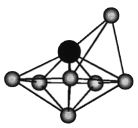	$E_g = -6184$ 25476 (25630) 26212 (26095) 29395 (29357)	$E_g = -7050$ 24130 (24266) 24927 (24826) 28470 (28436)
Sr^+Ar_8 (C_s)	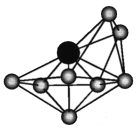	$E_g = -7210$ 25141 (25201) 26893 (26865) 30298 (30265)	$E_g = -8200$ 23554 (23609) 25432 (25406) 29243 (29214)

FIG. 4. The geometries of the absolute minima of the clusters Sr^+Ar_n, $n=2-8$. The two columns of numbers shown on the right hand are the energies of the absolute minima (E_g) and the vertical transition energies to the three $5p$ states; the first column for the ERFs, the second column for the mERFs. The numbers in parentheses are values obtained without including the spin–orbit coupling term, Eq. (12). Energy in cm^{-1}.

quenching the kinetic energy. For an accurate location of the stationary points we use the Newton–Raphson approach, whereas the computation of the harmonic frequencies reveals whether a stationary point is a minimum or a transition state.

V. RESULTS

A. Minimum energy structures

The number of stationary points increases rapidly with the size of cluster. In our case, however, the clusters are small enough to allow the location of the absolute minimum with some confidence. There are several methods to find stationary points on a multidimensional PES and their interconnectivity. In a recent article we have discussed and tested some of them for a Mg^+Ar_{12} cluster.[53]

Figure 4 shows the geometries of the absolute minima for the clusters with two to eight argon atoms. The binding energies, E_g, with respect to separated atoms, as well as the vertical energy differences between the ground state minimum and the three $5p$ states, are also tabulated in the same figure. The numbers in parentheses are the values without the spin–orbit coupling. The first column of numbers are the results with the ERFs fitted to the *ab initio* calculations. The second column represents the results of the mERFs. The binding energy of the cluster increases by 900–1000 cm^{-1}, with the addition of an argon atom as expected for a pair additive potential. We have also examined the role of the charge-induced dipole interaction terms in the potential. The charge-induced dipole interaction terms introduce many body effects, which, however, were found to be less important for the case of Sr^+–Ar than, for instance, in the case of Mg^+–Ar.[33]

The minimum energy structures of Sr^+Ar_2 and Sr^+Ar_3 have C_{2v} and C_{3v} symmetry, respectively. From the vertical transitions we can see the double degeneracy in the excited states of Sr^+Ar_3, a degeneracy that is removed when the spin–orbit coupling is included. Sr^+Ar_4 is also of C_{2v} symmetry with two trigonal pyramids sharing a common face. The next cluster has four argon atom on a plane, one argon atom below and the metal cation above. This structure has a plane of symmetry (C_s).

It is interesting to note that the structure of Sr^+Ar_5 is a precursor of the familiar structure of Sr^+Ar_6. By adding one more argon atom, a regular pentagon is formed with the sixth Ar below the plane and Sr^+ above, such that they form a configuration of C_{5v} symmetry. This configuration also supports a doubly degenerate level, as we can see from the vertical transition energies in the parentheses of Fig. 4. For Sr^+Ar_5, the closeness of its geometry to that of Sr^+Ar_6 results in an almost doubly degenerate level. For the ERF case, the vertical potential differences without spin–orbit coupling are 27 250 and 27 730 cm^{-1}.

Larger clusters are built by adding argon atoms above the centers of the triangular faces of Sr^+Ar_6, as is shown in Fig. 4. The positions of the argon atoms that start forming the second shell of the complex are guided by maximizing the number of Ar–Ar interactions.

The employment of the mERF to describe the Sr^+Ar interactions increases the well depth, but decreases the vertical energy differences among ground and excited states. Using the mERF potentials we find the largest harmonic frequency of the clusters to increase from 49.5 cm^{-1} in the dimer to 69.2 cm^{-1} in Sr^+Ar_8. The lowest frequency decreases from 27.3 to 12.9 cm^{-1}, but not in a monotonic fashion with the size of the cluster. The lowest harmonic frequency was found for Sr^+Ar_7.

B. Temperature dependence of the spectra

As was mentioned earlier, there is no indication in the experiment of how hot the clusters are when they are isolated and interact with the laser. It is therefore of interest to study the temperature dependence of the simulated spectra before comparing them with the experiment. We first performed simulations in the temperature range of 10–60 K with the ERF potentials. Figure 5 shows how the spectra are broadened by increasing T.

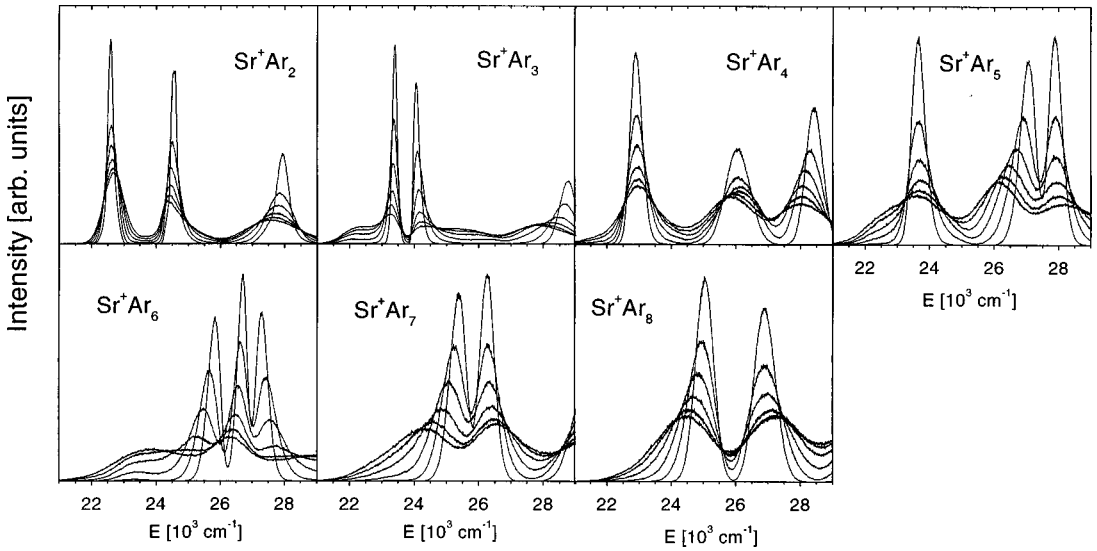

FIG. 5. Simulated spectra at several temperatures. For each cluster the shown curves correspond to the temperatures $T=10,20,30,40,50,60$ K with the intensities of the peaks decreasing as the temperature increases.

No significant shifts of the peaks with temperature are found for Sr^+Ar_2. From the three bands, the largest broadening is shown for the highest peak at 28 000 cm^{-1}. Larger clusters show variations in the first and/or second band for $T>30$ K. The most noticeable changes occur for the high symmetry clusters, Sr^+Ar_3 and Sr^+Ar_6. For these clusters we observe a sharp splitting of the doubly degenerate states at low temperatures, a feature that is expected exactly at the configurations with C_{3v} and C_{5v} symmetry. The splitting of the degenerate states is always found in our calculations because of the spin–orbit coupling term that destroys the degeneracy, but also the probability of picking up configurations of such high symmetry during the time integration of the trajectories is negligible.

For the aggregates with three, five, and six argon atoms we can see that a small peak starts appearing between 22 000 and 23 500 cm^{-1}, whose intensity increases with temperature. These spectral features may be due to other stationary points either in the ground or in the excited states. Analysis of the dynamics revealed related topographical characteristics in the ground state PES. For example, Fig. 6(a) shows the geometry of a second-order transition state for Sr^+Ar_3 with all atoms in a plane. In the neighborhood of this configuration the cluster spends considerable time and the energy differences with the first excited state are such that can produce a distinguishable new peak.

For Sr^+Ar_6 we found two relative local minima formed by moving one of the five argon atoms of the pentagon out of plane, as shown in Figs. 6(b) and 6(c). The minimum of Fig. 6(c) is responsible for the appearance of the shoulder in the spectrum shown in Fig. 5. On the other hand, transitions between the [Fig. 6(b)] minimum and the first excited state (at about 26 000 cm^{-1}) are hidden in the existing second band. However, such transitions are expected to enhance the intensity of this band, a fact that is actually observed in Fig. 5.

The existence of relative minima where the system spends appreciable time is responsible, not only for the secondary peaks in the spectra, but for the broadening of the existing ones. We, however, point out that comparison of the classical simulations with the experiment is valid with the assumption that classical mechanics reasonably mimic quantum mechanics, and the regions where the classical trajectories are trapped are the same with the regions where the amplitude of the eigenfunctions is large. We postpone this discussion for later on and proceed to compare the simulated spectra with experiment.

C. Comparison with the experiment

We first compare our simulations to experiment at 30 K, since at this temperature an overall agreement was found

(a) 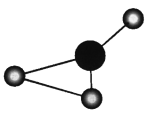	$E_g=-2218$ 21773 (21820) 23765 (23736) 30776 (30748)	$E_g=-2859$ 20841 (20882) 23053 (23028) 30897 (30881)
(b) 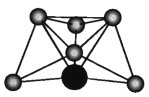	$E_g=-5164$ 26040 (26467) 26734 (26467) 27096 (26936)	$E_g=-5907$ 25013 (25428) 25695 (25428) 26129 (25981)
(c) 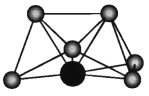	$E_g=-5160$ 23203 (23235) 26878 (26879) 29785 (29751)	$E_g=-5902$ 21789 (21817) 25914 (25916) 29134 (29104)

FIG. 6. The geometries of secondary stationary points in the ground electronic state of Sr^+Ar_3 (a) (a transition state), and Sr^+Ar_6 (b),(c) (relative minima), which cause the appearance of secondary peaks in the spectra as the temperature in the simulation increases. The two columns of numbers shown on the right hand are the energies of the absolute minimum and the vertical transitions to the three $5p$ states; the first column for the ERFs, the second column for the mERFs. The numbers in parentheses are values obtained without the spin–orbit interaction term [Eq. (12)].

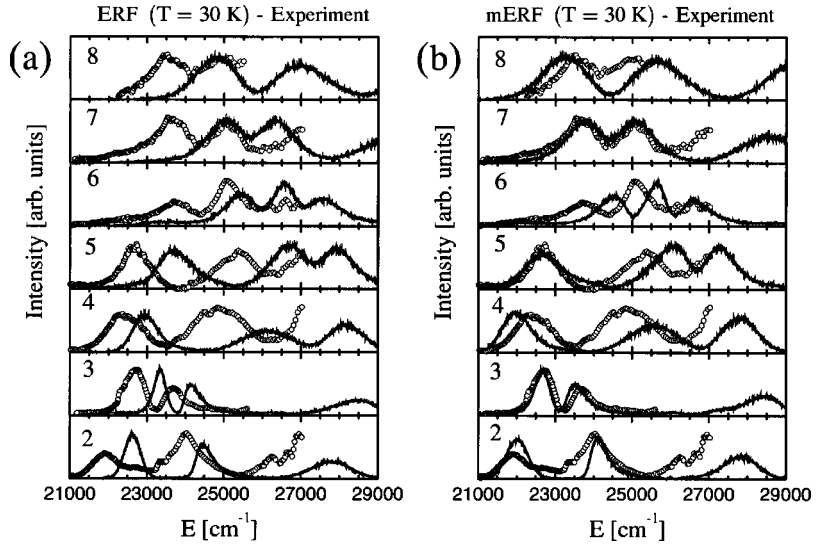

FIG. 7. A comparison of experimental to calculated spectra of Sr^+Ar_n, $n=2-8$, clusters at 30 K. In (a) the ERFs are used, whereas in (b) the modified ERFs are employed (see the text). Axes are as in Fig. 2.

between measured and computed spectra. Comparisons for other temperatures are left for later on. The experimental and simulated spectra at 30 K with the ERF potential are shown in Fig. 7(a). The open circles are the experimental spectra, whereas the results of the binning process in the classical trajectories appear as solid lines. We can see a persistent shift of all calculated spectra to the right for all clusters. It is about 500 cm^{-1} in the first band of Sr^+Ar_2 and increases with the size of the complex. The largest discrepancy is observed for Sr^+Ar_6 for which the difference between experimental and theoretical peaks is about 2000 cm^{-1}.

In spite of these dispositions, the trends marked in the experimental spectra and discussed in Sec. II are well reproduced. We do find significant blue shifts in the first peaks of Sr^+Ar_3 and Sr^+Ar_6 aggregates and red shifts in the second peaks for the other clusters. In particular, the proximity of the first two bands in the clusters with high symmetry is found and it is attributed to the splitting of the doubly degenerate states expected for C_{3v} and C_{5v} configurations.

The rather systematic shifts among calculated and experimental spectra led us to investigate spectra produced with the mERFs. As was discussed earlier, the mERF potentials show smaller vertical differences among the ground and excited states. The calculations with the mERFs were performed for the same temperature range, 10–60 K. The results of these simulations at 30 K are compared with the recorded spectra in Fig. 7(b).

The improvement in the position of absorption bands is now clear. For some clusters the agreement between the experimental and computed intensities is surprisingly good, particularly for the first band. As before, the largest disagreement is found for Sr^+Ar_6, but now the shift of the first peak in the calculated spectrum has been reduced from 2000 to 800 cm^{-1}. The expected trends in the first two absorption bands with the size of clusters are also well reproduced.

Making comparisons with the experimental spectra at 30 K does not, of course, mean that good agreement implies that the cluster has the same temperature. First of all, the simulations are carried out with zero total angular momentum. Also, as was previously noted, the temperature of the individual clusters at the experimental conditions is not known, and what is most probable is that the spectra are averages over several temperatures. However, it is worth comparing simulated to experimental spectra in order to see how the positions and widths of the absorption bands vary with temperature. In Fig. 8 we compare spectra at 10 K [Fig. 8(a)] and 50 K [Fig. 8(b)] using the simulations with the mERF. For $T<30$ K the bands become even narrower, while for $T>30$ K broader. Without a doubt, more detailed comparisons could be made by monitoring the temperature of each cluster separately.

VI. DISCUSSION

Before discussing the results presented in the previous sections, we devote some discussion to the accuracy of the model used to derive the PESs. As noted earlier, we have employed a pairwise additive potential function for the ground state of all clusters and a diatomic-in-molecules approach for the excited states.

In order to test the accuracy of the pairwise additive potential function we compare it with the results of *ab initio* calculations for the Sr^+Ar_2 and Sr^+Ar_3 clusters. Full geometry optimizations were performed at the RCCSD(T) level of theory, with the basis sets listed in Sec. IV A. During these calculations we correlated the $4s$, $4p$, and $5s$ electrons of Sr and the $3s$ and $3p$ electrons of each Ar atom in the cluster. For Sr^+Ar_3 this amounts, for example, to correlating 33 electrons. The bent minimum geometry of Sr^+Ar_2 found with the pairwise additive potential was also accurately reproduced at the RCCD(T) level of theory. Its energy with respect to the separated atoms is -1477 cm^{-1}, in good agreement with the value of -1508 cm^{-1} obtained with the ERF potential (cf. Fig. 4). The linear configuration of Sr^+Ar_2 is a transition state lying only 37 cm^{-1} above the bent minimum. The C_{3v} minimum of the Sr^+Ar_3 cluster was computed at E_g

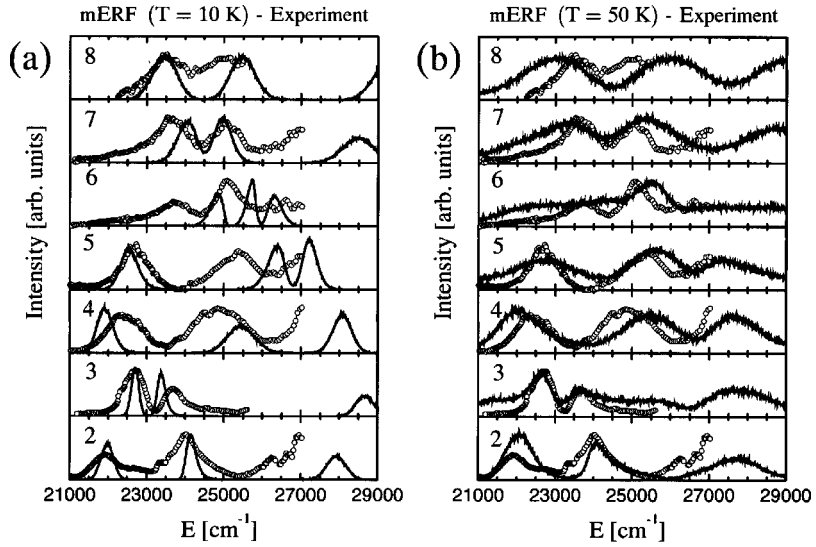

FIG. 8. A comparison of experimental to calculated spectra using the mERF potentials for Sr^+Ar_n, $n=2-8$, clusters at two temperatures; (a) 10 K and (b) 50 K. Axes are as in Fig. 2.

$=-2386$ cm^{-1}, also in good agreement with the value of -2411 cm^{-1} obtained with the ERF potential (Fig. 4).

The adequacy of expressing the ground state potentials as a sum of all diatomic contributions in the cluster has been further tested in our model by including the charge-induced dipole interaction terms, which are expected to be the most important for the metal ion doped argon clusters. The electrostatic nature of the bond in the ground state PES of Sr^+Ar was one of the conclusions in the *ab initio* study of the dimer.[2] The charge-induced dipole terms implicitly introduce many body effects in the cluster, and in some cases they may cause the appearance of new isomers through the balance of attractive and repulsive terms in the potential. An example is the Mg^+Ar_n[33,54] complexes, in which Mg^+ sits on the surface of the cluster, in addition to solvated forms predicted by a pair additive potential. In the case of strontium-argon clusters the charge-induced dipole interaction terms are not important. The larger bond lengths of Sr^+Ar make charge-induced dipole terms smaller. Thus, we believe that the ground state potential functions are adequately described by pair additive potentials.

For the excited states undoubtedly the one-electron approach leaves plenty of space for improvements. Since all-electron *ab initio* calculations are not feasible for the larger clusters, we must seek ways to improve the diatomic potentials that are the main ingredients of the model. As noted earlier, adjustment of the diatomic potential wells to the experimentally estimated values modified the simulated spectra. These kinds of improvements were obtained by keeping the same equilibrium distances for Sr^+Ar and the same repulsive potential for the $B\ ^2\Sigma$ state, as obtained by the *ab initio* calculations.[2] It should be emphasized that the *ab initio* calculations presented here are necessary in order to evaluate the equilibrium bond lengths for the ground and the excited states, as well as the shape of the repulsive $B\ ^2\Sigma$ state that are not available from experiment. It is conceivable that even more accurate *ab initio* calculations might further improve our results on the spectra.

The importance of the repulsive $B\ ^2\Sigma$ state in calculating the excited PES' can be seen from analytical expressions of the potentials, easily extracted for symmetric configurations. In the Appendix we tabulate the formulas of the V_{Sr^+Ar} interaction terms for C_{2v}, C_{3v}, and C_{5v} symmetry complexes. The blue shift in the first absorption band found for Sr^+Ar_3 could be foreseen by noting that the first state of Sr^+Ar_2 is described by just the Π state of the dimer, whereas in Sr^+Ar_3 the doubly degenerate state has a contribution from the Σ state. Similarly, for Sr^+Ar_6, we find a larger contribution of the V_Σ potential than in Sr^+Ar_4. Finally, the dominant role of the V_Σ potential in the nondegenerate states explains why these potentials move to higher energies. However, this does not mean that the potentials for the excited states of the clusters are repulsive all over the configuration space.

A way to visualize the blue shifts is to notice that for the C_{3v} and C_{5v} geometries the argon atom that is oriented along the $5p_z$ orbital of strontium causes an increase in the repulsive character of the potential. In the simplest case of the dimer the ground electronic state is formed by the overlap of s-type orbitals that results in a relatively weak bond. The doubly degenerate $A\ ^2\Pi$ state is attractive since the electron stays in a p-orbital perpendicular to the bond, a situation that causes a better exposure of the positive charge of the nucleus. The result is a shorter bond than the one in the ground state. When argon approaches strontium along the p_z orbital where the electron sits, the forces are repulsive $(B\ ^2\Sigma)$.

In a similar way, we can explain the behavior of the excited PES' in Sr^+Ar_6. In Fig. 9, we plot the three potentials originated from the $5p$ orbitals of strontium with the distance of strontium from the argon atom that is off the plane [Fig.9(a)], transformations that preserve the C_{5v} sym-

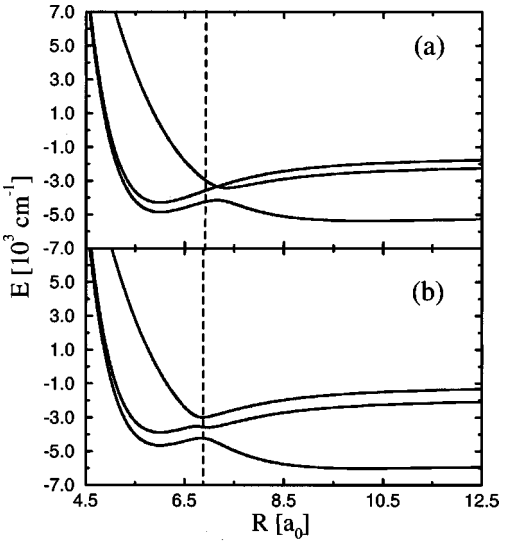

FIG. 9. Potential curves for the three excited $5p$ states of Sr^+Ar_6 as functions of the strontium-argon distance for (a) the argon atom off the pentagon plane, and (b) the distance of one argon atom in the pentagon plane. The dashed lines in the two figures mark the strontium-argon distances at the equilibrium point of the ground state from where the Franck–Condon transitions occur.

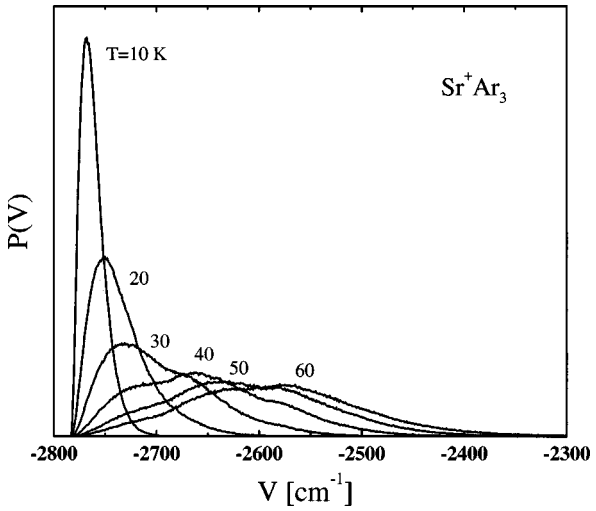

FIG. 10. Distributions of potential energies of Sr^+Ar_3 in its ground electronic state at several temperatures. A bimodal structure for temperatures above 30 K can be seen.

metry of the complex, and with respect to the distance from one of the argons in the plane [Fig. 9(b)]. In Fig. 9(a) it is seen that as R increases beyond the equilibrium distance, the repulsive potential decreases, but the attractive ones increase. This leads to a crossing with one of the two attractive potential curves and in an avoided crossing with the other. In Fig. 9(b), where one of the five plane argon atoms is moving, the C_{5v} symmetry is not kept, and thus, a second avoided crossing is found. At the distances where the Franck–Condon transition occurs (marked by the dashed lines in Fig. 9) the three potential surfaces approach one another in accord with the recorded photofragmentation spectra.

To summarize, we believe that improving the V_Σ and V_Π potentials of the dimer will result in better PES' of the complexes, even in the one-electron perturbative approximation.

The second component of the theory is the dynamics for simulating the photofragmentation spectra. Here, several assumptions are involved. The assumption of a constant, independent of the coordinates transition dipole moment operator is widely used in the literature, and we apply it here as well. The classical mechanical approach to calculate the photofragmentation spectra is the most severe approximation. First of all, to replace the configurational probability density function [P, Eq. (16)] in the upper surface with a distribution on the ground state, obtained by running classical trajectories, assumes a good correspondence between classical and quantum mechanics, something that is not known in advance because of the strong nonlinearities in the potential functions.[55] In other words, we assume that the same configuration space is covered by the quantum probability density as the classical trajectories in the simulations. This assumption is not unreasonable when averaged quantities are computed and compared with experiments or quantum mechanical calculations, as was found in numerous studies in the past. Thus, we expect that the total fragmentation cross sections averaged over several energies diminish the chances for a fortuitous agreement.

The dynamics were carried out at constant temperatures and among the six temperatures studied (10–60 K), the spectra at 30 K were found to be the most satisfactory. It is believed that clusters with different sizes had different temperatures during the recording of a spectrum, especially if we take into account that some experiments lasted several weeks. The fact that the broad characteristics, even the relative intensities for some sizes, are well reproduced by the simulations, does not support any speculations regarding the temperature of the clusters. Furthermore, spectral intensities are the most difficult quantities to reproduce in classical mechanical calculations.

Secondary peaks found above some temperatures have been attributed to topographical characteristics on the ground electronic potential surface. The most pronounced are those for Sr^+Ar_3 and Sr^+Ar_6. The complex is trapped to relative stationary points for an extended time interval, and this causes the appearance of secondary bands. For Sr^+Ar_3 the trapping is due to a transition state and to the small forces out of plane. The spectral peak appears at 22 000 cm^{-1} (Fig. 5). For Sr^+Ar_6, the relative minima shown in Fig. 6 are responsible for the peak at 23 000 cm^{-1}. In the latter case it is worth pointing out that a similar broadening is observed in the experimental spectrum (Fig. 2).

The relative stationary points on the PES' show up when we plot distributions of the potential energy calculated from the trajectories in the ground surface. The most pronounced of them is shown in Fig. 10 for Sr^+Ar_3. Above 30 K, a bimodal distribution starts appearing as a result of the trapping of the trajectory at the transition state region. We believe that the Nosé–Hoover method, which generates canonical ensembles, is appropriate for the present study.

Broad spectra without any vibrational structure have been found, even for the smallest complex with two argon atoms. The small harmonic frequencies and the floppiness of

these clusters would give large densities of states. This, combined with the fact that the clusters may be hot during their photofragmentation, could explain the unstructured broadbands. However, it is difficult to state at present any firm reason for this behavior since nothing is known about the mechanism of photodissociation. How does the complex break? It could be by the absorption of a second photon to reach higher states from where the aggregate is fragmented or it could come down to the ground state after several oscillations of the wave packet on the upper surface. We do not know the topographies of those excited states that correlate with the $4d$ orbitals of strontium. They could cross the higher states, and, thus, predissociation could occur via them. To answer such important questions we are currently studying the photofragmentation of Sr^+Ar_2 in more detail; these results will be the subject of a future publication.

VII. CONCLUSIONS

Experiment and theory are combined in an effort to extract the structures and dynamics of Sr^+Ar_n, $n=2-8$, clusters through the study of the photodissociation spectra. The total photofragmentation cross sections have been recorded in a time of flight mass spectrometer. The complexes are formed in a laser vaporization source after which a size selected cluster interacts with a laser field leading to its fragmentation. We assume that total absorption cross sections are equal to the total photofragmentation cross sections. The theory that simulates the total absorption spectra is carried out at the classical mechanical level and the excited potential energy surfaces are computed with a one-electron perturbative model. The necessary ingredients for this model, namely, the potential curves for $A\ ^2\Pi$ and $B\ ^2\Sigma$ states of the dimer, have been constructed from *ab initio* calculations. For the ground state potential energy surfaces a pair additive approach is adopted. Employing the Nosé–Hoover scheme the dynamics are carried out in canonical ensembles and for the temperature range of 10–60 K.

The main conclusions of this study are the following.

In the energy range of 21 000 to 29 000 cm^{-1}, three absorption bands are observed for all clusters studied , which are attributed to transitions from the ground to the three excited states that correlate to the $5p$ orbitals of strontium.

No vibrational structure is found in the recorded spectra, even by increasing the resolution to 1 cm^{-1} in some regions of the spectrum.

The theoretical spectra computed with the Extended Rydberg Functions fitted to the *ab initio* calculations reproduce the patterns and trends of the experimental spectra, but they are shifted to higher frequencies. A better agreement is achieved by adjusting the depth of potential wells of the ground and excited $A\ ^2\Pi$ state of the dimer to the experimentally estimated values.

Sr^+Ar_3 is a trigonal pyramid of C_{3v} symmetry and Sr^+Ar_6 has a C_{5v} symmetry with five argon atoms forming a regular pentagon, one argon atom below and the cation above the pentagon plane. For both clusters theory reproduces the characteristic blue shifts in the absorption spectra and the splittings of the doubly degenerate states predicted for these symmetric complexes.

ACKNOWLEDGMENTS

Financial support from the Hellenic General Secretariat for Research and Technology under the program for support of scientific staff ΠΕΝΕΔ - 1994 (15774/296) is gratefully acknowledged. Support from the Ultraviolet Laser Facility (Contract No. ERB-CHGE-CT920007) operating at FORTH is also acknowledged. Part of this work was performed under the auspices of the Division of Chemical Sciences, Office of Basic Energy Sciences, U.S. Department of Energy under Contract No. DE-AC06-76RLO 1830 with Battelle Memorial Institute, which operates the Pacific Northwest National Laboratory. Computer resources were provided by the Division of Chemical Sciences and by the Scientific Computing Staff, Office of Energy Research, at the National Energy Research Supercomputer Center (Berkeley, CA).

APPENDIX: ANALYTICAL POTENTIAL FUNCTIONS OF Sr^+Ar_n

For the symmetric configurations of the complexes it is possible to extract analytical formulas for the excited potential surfaces. In the following we give the strontium–argon interactions of the three excited PES'. The complete potential functions are formed by adding the Ar–Ar pair potentials.

We define the parameter A

$$A=-(3\cos^2\gamma-1). \tag{A1}$$

γ is the angle between one bond length of Sr^+Ar and the symmetry axis of the complex

1. Sr^+Ar_2 (C_{2v})

$$E_1=2V_\Pi, \tag{A2}$$

$$E_2=\tfrac{2}{3}[V_\Sigma(2+A)+V_\Pi(1-A)], \tag{A3}$$

$$E_3=\tfrac{2}{3}[V_\Sigma(1-A)+V_\Pi(2+A)]. \tag{A4}$$

2. Sr^+Ar_3 (C_{3v})

$$E_{1,2}=V_\Sigma(1+A/2)+V_\Pi(2-A/2), \tag{A5}$$

$$E_3=V_\Sigma(1-A)+V_\Pi(2+A). \tag{A6}$$

3. Sr^+Ar_4 (C_{2v})

$$E_1=2V_\Pi^{(1)}+\tfrac{2}{3}[V_\Sigma^{(2)}(2+A_2)+V_\Pi^{(2)}(1-A_2)], \tag{A7}$$

$$E_2=2V_\Pi^{(2)}+\tfrac{2}{3}[V_\Sigma^{(1)}(2+A_1)+V_\Pi^{(1)}(1-A_1)], \tag{A8}$$

$$E_3=\tfrac{2}{3}[V_\Sigma^{(1)}(1-A_1)+V_\Pi^{(1)}(2+A_1)+V_\Sigma^{(2)}(1-A_2)+V_\Pi^{(2)}(2+A_2)]. \tag{A9}$$

In this case, we define two angles, and therefore two A parameters. The numbers 1 and 2 denote the two different angles formed by the C_{2v} axis and the bond lengths of Sr^+Ar with one Ar in the two different diagonal positions (see Fig. 4).

4. Sr^+Ar_6 (C_{5v})

$$E_{1,2}=V_{\Pi}^{(1)}+\tfrac{5}{3}[V_{\Sigma}^{(2)}(1+A/2)+V_{\Pi}^{(2)}(2-A/2)], \qquad \text{(A10)}$$

$$E_3=V_{\Sigma}^{(1)}+\tfrac{5}{3}[V_{\Sigma}^{(2)}(1-A)+V_{\Pi}^{(2)}(2+A)]. \qquad \text{(A11)}$$

1 denotes the diatomic potentials of strontium with the argon atom below the pentagon plane and 2 the diatomic potentials with the argons on the plane (see Fig. 4).

[1] C. Lüder and M. Velegrakis, J. Chem. Phys. **105**, 2167 (1996).
[2] S. S. Xantheas, G. S. Fanourgakis, S. C. Farantos, and M. Velegrakis, J. Chem. Phys. **108**, 46 (1998).
[3] A. A. Radzig and B. M. Smirnov, *Reference Data on Atoms, Molecules and Ions* (Springer-Verlag, Berlin, 1985).
[4] J. A. Coxon, W. E. Jones, and K. V. Subbaram, Can. J. Phys. **53**, 2321 (1975).
[5] K. V. Subbaram, J. A. Coxon, and W. E. Jones, Can. J. Phys. **54**, 1535 (1976).
[6] D. C. Hartman and J. S. Winn, J. Chem. Phys. **74**, 4320 (1981).
[7] J. G. McCaffrey, D. J. Funk, and W. Breckenridge, J. Chem. Phys. **100**, 955 (1993).
[8] J. S. Pilgrim, C. S. Yeh, K. R. Berry, and M. A. Duncan, J. Chem. Phys. **101**, 7945 (1994).
[9] S. I. Panov, J. M. Williamson, and T. A. Miller, J. Chem. Phys. **102**, 7359 (1995).
[10] T. Buthelezi, D. Bellert, V. Lewis, and P. J. Brucat, Chem. Phys. Lett. **246**, 145 (1995).
[11] M. A. Duncan, Annu. Rev. Phys. Chem. **48**, 69 (1997).
[12] C. W. Bauschlicher, Jr., in *Advances in Metal and Semiconductor Clusters*, edited by M. A. Duncan (JAI Press, London, 1994), Vol. 2, p. 165.
[13] H. Partridge, C. W. Bauschlicher, Jr., and S. R. Langhoff, J. Phys. Chem. **96**, 5350 (1992).
[14] C. W. Bauschlicher, Jr. and H. Partridge, Chem. Phys. Lett. **239**, 241 (1995).
[15] R. J. Le Roy, J. Chem. Phys. **101**, 10 217 (1994).
[16] S. Martrenchard-Barra, C. Dedonder-Lardeux, C. Jouvet, and D. Solgadi, J. Chem. Phys. **98**, 528 (1993).
[17] C. Lüder, D. Prekas, A. Vourliotaki, and M. Velegrakis, Chem. Phys. Lett. **267**, 149 (1997).
[18] D. Prekas, B.-H. Feng, and M. Velegrakis, J. Chem. Phys. **108**, 2712 (1998).
[19] S. G. Donnelly, C. A. Shuttenmaer, J. Qian, and J. M. Farrar, J. Chem. Soc. Faraday Trans. **89**, 1457 (1993).
[20] S. G. Donnelly and J. M. Farrar, J. Chem. Phys. **98**, 5450 (1993).
[21] M. Sanekata, F. Misaizu, K. Fuke, and S. Iwata, J. Chem. Phys. **104**, 9768 (1996).
[22] F. Misaizu, M. Sanekata, K. Fuke, and S. Iwata, J. Chem. Phys. **100**, 1161 (1994).
[23] W. C. Wiley and I. H. McLaren, Rev. Sci. Instrum. **26**, 1150 (1955).
[24] W. E. Baylis, J. Phys. B **10**, L477 (1977).
[25] L. C. Balling and J. J. Wright, J. Chem. Phys. **79**, 2941 (1983).
[26] H. Harima, T. Ihara, Y. Uramo, and K. Tachibana, Phys. Rev. A **34**, 2911 (1986).
[27] J. A. Boatz and M. E. Fajardo, J. Chem. Phys. **101**, 3472 (1994).
[28] W. G. Lawrence and V. A. Apkarian, J. Chem. Phys. **101**, 1820 (1994).
[29] M. H. Alexander, A. R. Walton, M. Yang, X. Yang, E. Hwang, and P. J. Dagdigian, J. Chem. Phys. **106**, 6320 (1997).
[30] V. Aquilanti and G. Grossi, J. Chem. Phys. **73**, 1165 (1980).
[31] In the matrix given in the appendix of Ref. 28, the matrix element (2,3) should be $(\frac{1}{3}V_{01}-\frac{2}{3}V_{-10})$.
[32] R. A. Aziz and M. J. Slaman, Mol. Phys. **58**, 679 (1986).
[33] G. S. Fanourgakis and S. C. Farantos, J. Phys. Chem. **100**, 3900 (1996).
[34] H.-J. Werner and P. Knowles, J. Chem. Phys. **89**, 5803 (1988).
[35] H.-J. Werner and P. Knowles, Chem. Phys. Lett. **245**, 514 (1988).
[36] H.-J. Werner and E. Reinsch, J. Chem. Phys. **76**, 3144 (1982).
[37] H.-J. Werner, Adv. Chem. Phys. **LXIX**, 1 (1987).
[38] M. Kaupp, P. V. R. Schleyer, H. Stoll, and H. Preuss, J. Chem. Phys. **94**, 1360 (1991).
[39] D. E. Woon and J. T. H. Dunning, J. Chem. Phys. **100**, 2975 (1994).
[40] D. E. Woon and J. T. H. Dunning, J. Chem. Phys. **98**, 1358 (1993).
[41] R. A. Kendall, J. T. H. Dunning, and R. J. Harrison, J. Chem. Phys. **96**, 6796 (1992).
[42] J. T. H. Dunning, J. Chem. Phys. **90**, 1007 (1989).
[43] MOLPRO is a package of *ab initio* programs written by H.-J. Werner and P. J. Knowles, with contributions from J. Almlf, R. D. Amos, A. Berning, D. L. Cooper, M. J. O. Deegan, F. Eckert, S. T. Elbert, C. Hampel, R. Lindh, W. Meyer, M. E. Mura, A. Nicklass, K. Peterson, R. Pitzer, P. Pulay, M. Shltz, H. Stoll, A. J. Stone, P. R. Taylor, and T. Thorsteinsson. For the RCCSD(T) implementation in MOLPRO, see P. J. Knowles, C. Hampel, and H.-J. Werner, J. Chem. Phys. **99**, 5219 (1993).
[44] J. N. Murrell, S. Carter, S. C. Farantos, P. Huxley, and A. J. C. Varandas, *Molecular Potential Energy Functions* (Wiley, New York, 1984).
[45] M. R. Blomberg and P. E. M. Siegbahn, Int. J. Quantum Chem. **8**, 61 (1974).
[46] S. R. Langhoff and E. R. Davidson, J. Chem. Phys. **78**, 5682 (1983).
[47] E. A. Gislason, J. Chem. Phys. **58**, 3702 (1973).
[48] M. Lax, J. Chem. Phys. **20**, 1752 (1952).
[49] E. J. Heller, J. Chem. Phys. **68**, 2066 (1978).
[50] S. Nosé, Mol. Phys. **52**, 255 (1984).
[51] S. Nosé, J. Chem. Phys. **81**, 511 (1984).
[52] W. G. Hoover, Phys. Rev. A **31**, 1695 (1985).
[53] J. Papadakis, G. S. Fanourgakis, S. C. Farantos, and M. Founargiotakis, J. Comput. Chem. **18**, 1011 (1997).
[54] G. S. Fanourgakis, S. C. Farantos, P. Parneix, and P. Bréchignac, J. Chem. Phys. **106**, 4954 (1997).
[55] S. C. Farantos, Int. Rev. Phys. Chem. **15**, 345 (1996).